Dynamically Linking Influenza Virus Infection with Lung Injury to Predict Disease Severity

Margaret A. Myers[1], Amanda P. Smith[1], Lindey C. Lane[1], David J. Moquin[2], Peter Vogel[3], Stacie Woolard[4], Amber M. Smith[1*]

[1] Department of Pediatrics, University of Tennessee Health Science Center, Memphis, TN 38163, USA
[2] Department of Anesthesiology, Washington University School of Medicine, St. Louis, MO 63110 USA
[3] Department of Pathology, St. Jude Children's Research Hospital, Memphis, TN 38105, USA
[4] Flow Cytometry Core, St. Jude Children's Research Hospital, Memphis, TN 38105, USA

* amber.smith@uthsc.edu

Abstract

Influenza viruses cause a significant amount of morbidity and mortality. Understanding host immune control efficacy and how different factors influence acute lung injury and disease severity are critical. Here, we established the dynamical connections between viral loads, infected cells, $CD8^+$ T cells, lung injury, and disease severity using an integrative model-experiment exchange. The model predicts that infection resolution is sensitive to CD8 expansion, that there is a critical T cell magnitude needed for efficient resolution, and that the rate of T cell-mediated clearance is dependent on infected cell density. We used whole lung histomorphometry to validate the model, which showed that the infected area matched the model-predicted infected cell dynamics, and that the resolved area paralleled the relative CD8 dynamics. Additional analysis revealed a nonlinear relation between disease severity (i.e., weight loss) and lung injury. These novel links between important pathogen kinetics and host pathology enhance our ability to forecast disease progression, potential complications, and therapeutic efficacy.

Introduction

Over 15 million respiratory infections and 200,000 hospitalizations result from influenza A viruses (IAVs) each year [1–4]. The incidence and severity of IAV infections increases when new strains emerge and/or when there is a lack of prior immunity. A robust immune response is crucial for resolving viral infections, but immune-mediated pathology can exacerbate disease [5–9]. High viral loads also play a role in disease progression [10], but these do not always correlate with the strength of the host response or with disease severity [11–14]. An understanding of how viral loads, host immune responses, and disease progression are related is critical to identify disease-specific markers that may help predict hospitalization or other complications.

During IAV infection, viral loads increase rapidly for the first 1-2 days of infection before reaching a peak (e.g., as in [13, 15–19]). In naïve hosts, viral loads then begin to decline, first slowly (< 1 $\log_{10}$ TCID_{50}/d; 3–7 d) then rapidly ($4-5$ $\log_{10}$ TCID_{50}/d; 7–9 d) [15]. We previously quantified this biphasic viral decline with a mathematical model, which indicated that the rate of infected cell clearance increases as the density of infected cells decreases [15]. The timing of the second, rapid viral decay phase coincides with the expansion of $CD8^+$ T cells, which are the primary cell responsible for clearing infected cells and resolving the infection [20–24],

and, to a lesser extent, neutralizing antibodies [21, 22, 24–26]. For the $CD8^+$ T cell response, in particular, it remains unclear whether the efficacy of these cells is dictated by their own density [27, 28], infected cell density [29–31], or both [32]. While quantifying $CD8^+$ T cell efficacy is difficult *in vitro* and *in vivo*, the question is ripe for *in silico* investigation. Indeed, several modeling studies have described $CD8^+$ T cell-mediated infected cell clearance for various viral infections, including IAV, HIV, and LCMV (e.g., as in [17,27,29,32–38]). However, for IAV infections, nonlinearities in the efficiency of the $CD8^+$ T cell response and the consequences on viral loads and host pathology have not yet been investigated in detail.

A better understanding of infected cell clearance may also yield insight into the damage induced to the lung during IAV infection. In general, widespread alveolar disease is observed in patients who succumb to the infection [39]. Further, hospitalized patients that died as a result from infection with the 2009 H1N1 influenza virus had large numbers of $CD8^+$ T cells present in their lung tissue [7]. Large pulmonary populations of $CD8^+$ T cells do contribute to lung injury by targeting IAV-infected cells (reviewed in [5]) in addition to 'bystander damage' to uninfected epithelial cells [40]. The accumulation of damage to the epithelium during IAV infection, either from virally-induced cell lysis or immune-mediated effects, is relatively understudied. This is in part due to the difficulty in measuring the dynamics of infected cells and in establishing how damage correlates to different host responses. Recent technological advances, including the use of reporter viruses [41–44] and lung histomorphometry [12, 45–47], have provided an opportunity to acquire these types of measurements. However, even with these techniques, quantitative data over the course of infection is not currently available. Having data such as these should help reconcile potential nonlinearities in infected cell clearance and provide insight into the accumulated lung damage, which we hypothesize is a marker of disease severity.

In general, measures of disease severity do not seem to be directly correlated to viral loads or to specific immunological components. In humans infected with IAV, viral loads typically increase prior to the onset of systemic symptoms, which peak around 2–3 d post-infection (pi) [18,48,49]. Respiratory symptoms often last longer and can remain following viral clearance [48]. In the murine model, weight loss is used as an indicator of disease progression and severity, where greater weight loss corresponds to more severe disease [50–52]. Animal weights typically drop slowly in the first several days during an IAV infection and more rapidly as the infection begins to resolve [19, 53]. This is unlike viral load dynamics in these animals, which increase rapidly during the first 0–3 d pi then remain relatively constant prior to resolution [15]. Because weight loss often occurs following resolution of the infection, immune-mediated pathology is thought to

play a role [5, 52, 54–56]. Host and pathogen factors, such as age, viral proteins, and inoculum size, can also influence disease progression [13, 14, 57, 58]. While the causes of IAV-associated disease and mortality remain elusive, this gap in knowledge impairs our ability to effectively predict, understand, and treat the disease.

To gain deeper insight into the dynamics of viral resolution and investigate the connection between viral loads and disease severity, we simultaneously measured viral loads and $CD8^+$ T cells daily from the lungs of BALB/cJ mice infected with influenza A/Puerto Rico/8/34 (H1N1) (PR8). We then developed a model that describes their kinetics to explore the mechanisms and dynamics of $CD8^+$ T cell influx and their efficiency in removing virus-infected cells. The model verified our previous results that infected cells are cleared in a density-dependent manner. We further determined that infection duration is dependent on the magnitude of $CD8^+$ T cells rather than their efficacy. Exploring these findings through quantitative whole lung histomorphometry corroborated the model-predicted infected cell dynamics and the direct relation between infected cell clearance and $CD8^+$ T cell expansion. In addition, these data revealed a nonlinear connection between disease severity, as measured by weight loss, and the amount of the lung impacted by the infection. The data, model, and analyses provide a robust quantification of the density-dependent nature of $CD8^+$ T cell-mediated clearance, and the critical connections between these cells and the dynamics of viral loads, infected cells, lung injury, and disease severity.

Results

Virus and $CD8^+$ T cell kinetics

In animals infected with 75 $TCID_{50}$ PR8, virus rapidly infects cells or is cleared within 4 h pi (Figure 1). Virus then increases exponentially and peaks after ∼2 d pi. Following the peak, virus enters a biphasic decline. In the first phase (2–6 d pi), virus decays slowly and at a relatively constant rate (0.2 $\log_{10}$ $TCID_{50}$/d) [15]. In the second phase (7–8 d pi), virus is cleared rapidly with a loss of $4-5$ $\log_{10}$ $TCID_{50}$ in 1–2 d (average of -3.8 $\log_{10}$ $TCID_{50}$/d) [15]. $CD8^+$ T cells remain at their baseline level from 0–2 d pi before they infiltrate the lung tissue and increase slightly at 2–3 d pi. The population briefly contracts (3–5 d pi) before expanding rapidly (6–8 d pi). This expansion corresponds to the second viral decay phase. Sixty percent of mice clear the infection by 8 d pi, and the other forty percent by 9 d pi. $CD8^+$ T cells decline following viral clearance (8–10 d pi), but do not return to their baseline level. These cells then increase

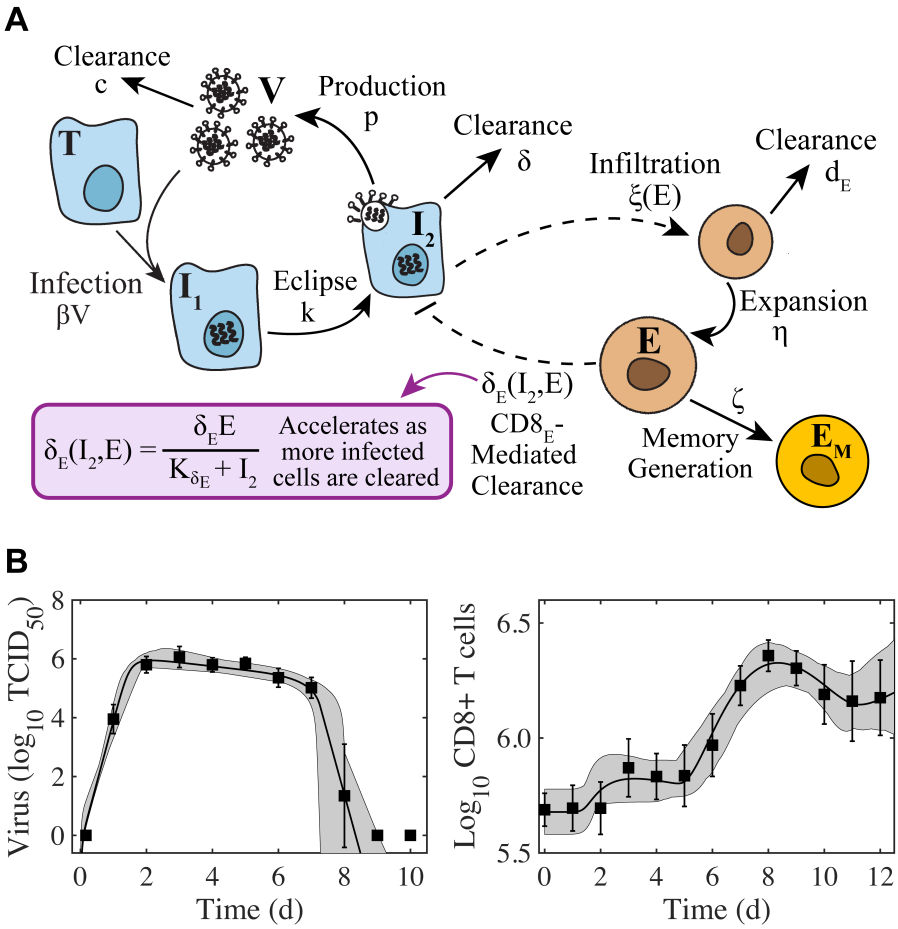

Figure 1. Schematic and fit of the CD8$^+$ T cell viral kinetic model. (A) Schematic of the CD8$^+$ T cell model in Equations (1)–(6). In the model, target cells (T) are infected at rate βV. Infected cells (I_1) undergo an eclipse phase and transition to become productively-infected cells (I_2) at rate k. Virus (V) is produced by infected cells at rate p a85d is cleared at rate c. Infected cells are cleared at rate δ by non-specific mechanisms and at rate $\delta_E(I_2, E)$ by effector CD8$^+$ T cells (E; denoted CD8$_\mathrm{E}$). The dashed lines represent interactions between infected cells and CD8$_\mathrm{E}$. CD8$_\mathrm{E}$ infiltration ($\xi(E) = \xi/(K_E + E)$) is proportional to infected cells and is limited by CD8$_\mathrm{E}$ with half-saturation constant K_E. CD8$_\mathrm{E}$ expansion (η) occurs proportional to infected cells τ_E days ago. Memory CD8$^+$ T cell (E_M; denoted CD8$_\mathrm{M}$) generation occurs at rate ζ and proportional to CD8$_\mathrm{E}$ τ_M days ago. (B) Fit of the CD8$^+$ T cell model (Equations (1)–(6)) to virus and CD8$^+$ T cells from the lungs of mice infected with 75 TCID$_{50}$ PR8 (10 mice per time point). The total number of CD8$^+$ T cells is $\hat{E} = E + E_M + \hat{E}_0$. The solid black line is the optimal solution and the gray shading is are the model solutions using parameter sets within the 95% CIs. Parameters are given in Table 1. Data are shown as mean ± standard deviation.

again slightly from 10–12 d pi.

Viral kinetic model with CD8$^+$ T cell-mediated clearance

We previously described the viral load kinetics and biphasic decline using a density-dependent (DD) model in Equations (S7)–(S10) (Supplementary Information) [15], which assumes that the rate of infected cell clearance increases as the density of infected cells decreases (i.e., $\delta_d(I_2) =$

$\delta_d/(K_\delta + I_2)$). Because the rapid decay of virus is thought to be due to the clearance of infected cells by CD8$^+$ T cells, we developed a model that describes the dynamics of these cells and their efficiency in resolving the infection (Equations (1)–(6); Figure 1A). The model includes equations for effector (E, denoted CD8$_\mathrm{E}$) and memory (E_M, denoted CD8$_\mathrm{M}$) CD8$^+$ T cells, and two mechanisms of infected cell clearance. During the first viral decay phase (2–6 d pi), the rate of infected cell clearance by unspecified mechanisms is relatively constant (δ). During the rapid, second viral decay phase (7–8 d pi), CD8$_\mathrm{E}$-mediated infected cell clearance occurs at a rate that increases as the density of infected cells decreases ($\delta_E(I_2, E) = \delta_E E/(K_{\delta_E} + I_2)$). Excluding this density dependence entirely resulted in a significant and premature decline in viral loads, which disagreed with the experimental data. We also tested whether the density dependence could be included in the CD8$^+$ T cell expansion rate rather than in the infected cell clearance rate (see Equations (S1)–(S6)) as other models have done (e.g., as in [59–61]). This modification yielded a close fit to the viral load and CD8$^+$ T cell data at 6–10 d pi but not at other time points (Figure S1). However, the viral load data was slightly underestimated at 7 d pi and the rapid decline between 7–8 d pi. Thus, retaining the density-dependence in the rate of infected cell clearance most accurately captured the entire dataset. Although memory CD8$^+$ T cells are not the focus here, it was necessary to include the CD8$_\mathrm{M}$ population because CD8$^+$ T cells are at a significantly higher level at 10–12 d pi than at 0 d pi (Figure 1B). The model includes terms for CD8$_\mathrm{E}$ infiltration ($\xi I_2/(K_E + E)$), which accounts for the initial increase at 2–3 d pi, and for CD8$_\mathrm{E}$ expansion ($\eta E I_2(t - \tau_E)$), which accounts for the larger increase between 5–8 d pi. To capture the contraction of CD8$^+$ T cells between these times (3–5 d pi), it was necessary to assume that CD8$_\mathrm{E}$ infiltration is reduced by their own population (i.e., $\xi(E) = \xi/(K_E + E)$). In both terms, the increase is proportional to the number of infected cells. Fitting the model simultaneously to viral loads and CD8$^+$ T cells from the lungs of infected animals illustrated the accuracy of the model (Figure 1B). The resulting parameter values, 95% confidence intervals (CIs), ensembles, and histograms are given in Table 1 and in Figures 2 and S2–S3.

Plotting the model ensembles revealed a correlation between the two infected cell clearance parameters (δ and δ_E; Figure 2B), which represent the efficacy of the non-specific immune response and the CD8$^+$ T cell response, respectively. Performing a sensitivity analysis showed that the viral load dynamics do not change substantially when these parameters are increased or decreased. However, decreasing the rate of non-specific infected cell clearance (i.e., lower δ) resulted in a significant increase in the number of CD8$_\mathrm{E}$ due to the small increase in the number of infected cells (Figures S4-S5). Even with a larger CD8$_\mathrm{E}$ population, recovery was

Table 1. CD8$^+$ T cell model parameters. Parameters and 95% confidence intervals obtained from fitting the CD8$^+$ T cell model (Equations (1)–(6)) to viral titers and CD8$^+$ T cells from mice infected with 75 $TCID_{50}$ PR8. $CD8_E$ and $CD8_M$ denote effector (E) and memory (E_M) CD8$^+$ T cells, respectively. The total number of CD8$^+$ T cells is $\hat{E} = E + E_M + \hat{E}_0$ and is denoted by CD8.

Parameter	Description	Units	Value	95% CI
β	Virus infectivity	$TCID_{50}^{-1}$ d^{-1}	6.2×10^{-5}	$[5.3 \times 10^{-6},\ 1.0 \times 10^{-4}]$
k	Eclipse phase transition	d^{-1}	4.0	[4.0, 6.0]
p	Virus production	$TCID_{50}$ $cell^{-1}$ d^{-1}	1.0	$[5.8 \times 10^{-1},\ 1.1 \times 10^{2}]$
c	Virus clearance	d^{-1}	9.4	$[5.6,\ 9.5 \times 10^{2}]$
δ	Infected cell clearance	d^{-1}	2.4×10^{-1}	$[1.0 \times 10^{-1},\ 6.6 \times 10^{-1}]$
δ_E	Infected cell clearance by $CD8_E$	cells $CD8_E^{-1}$ d^{-1}	1.9	$[3.3 \times 10^{-1},\ 2.0]$
K_{δ_E}	Half-saturation constant	cells	4.3×10^{2}	$[1.0 \times 10^{2},\ 2.9 \times 10^{5}]$
ξ	$CD8_E$ infiltration	$CD8_E^2$ $cell^{-1}$ d^{-1}	2.6×10^{4}	$[1.3 \times 10^{2},\ 8.7 \times 10^{4}]$
K_E	Half-saturation constant	$CD8_E$	8.1×10^{5}	$[1.0 \times 10^{3},\ 1.0 \times 10^{6}]$
η	$CD8_E$ expansion	$cell^{-1}$ d^{-1}	2.5×10^{-7}	$[1.6 \times 10^{-8},\ 6.7 \times 10^{-7}]$
τ_E	Delay in $CD8_E$ expansion	d	3.6	[2.1, 5.9]
d_E	$CD8_E$ clearance	d^{-1}	1.0	$[5.1 \times 10^{-2},\ 2.0]$
ζ	$CD8_M$ generation	$CD8_M$ $CD8_E^{-1}$ d^{-1}	2.2×10^{-1}	$[1.0 \times 10^{-2},\ 9.4 \times 10^{-1}]$
τ_M	Delay in $CD8_M$ generation	d	3.5	[3.0, 4.0]
$\hat{E}_0$	Baseline CD8	CD8	4.2×10^{5}	$[3.3 \times 10^{5},\ 5.3 \times 10^{5}]$
$T(0)$	Initial uninfected cells	cells	1×10^{7}	-
$I_1(0)$	Initial infected cells	cells	75	-
$I_2(0)$	Initial infected cells	cells	0	-
$V(0)$	Initial virus	$TCID_{50}$	0	-
$E(0)$	Initial $CD8_E$	$CD8_E$	0	-
$E_M(0)$	Initial $CD8_M$	$CD8_M$	0	-

delayed by only ~ 0.1 d. Given the correlation between δ and δ_E (Figure 2B), a more efficient $CD8_E$ response (i.e., higher δ_E) may be able to overcome this short delay in resolution. The lack of sensitivity to changes in the infected cell clearance parameters is in contrast to the DD model, where the viral dynamics were most sensitive to perturbations in δ_d (Figure S4) [15], which encompasses multiple processes. With CD8$^+$ T cells explicitly included in the model, the infection duration was most sensitive to changes in the rate of $CD8_E$ expansion (η) (Figures S4, S5; discussed in more detail below).

Examining the parameter ensembles and sensitivity analysis also yielded insight into how other model parameters affect the CD8$^+$ T cell response. The rates of $CD8_E$ expansion (η) and clearance (d_E) were slightly correlated, indicating a balance between these two processes (Figure 2C). This correlation and the sensitivity of η produced model dynamics that were also sensitive to changes in the $CD8_E$ clearance rate (d_E) (Figure S6). As expected, the rates of $CD8_M$ generation (ζ) and $CD8_E$ clearance (d_E) were correlated (Figure 2C). It has been estimated that approximately 5–10% of effector CD8$^+$ T cells survive to become a long-lasting memory population [62]. Despite the inability to distinguish between $CD8_E$ and $CD8_M$ in

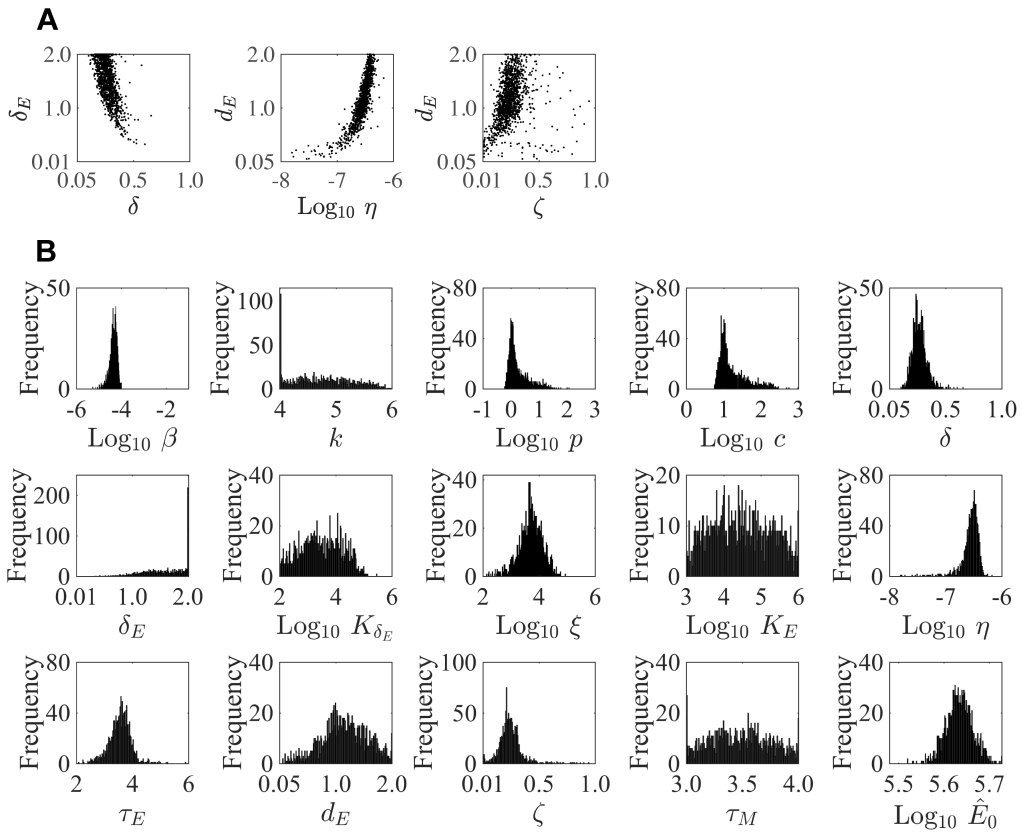

Figure 2. Parameter ensembles and histograms. Parameter ensembles (Panels A) and histograms (Panel B) resulting from fitting the CD8$^+$ T cell viral kinetic model (Equations (1)–(6)) to viral titers and CD8$^+$ T cells from mice infected with 75 TCID_{50} PR8. (A) The rates of infected cell clearance by non-specific mechanisms (δ) and by CD8_E (δ_E) are slightly negatively correlated. Correlations were also present between the rates of CD8_E clearance (d_E), CD8_E expansion (η), and CD8_M generation (ζ). The axes limits reflect imposed bounds. Additional ensemble plots are in Figures S2–S3. (B) The histograms show that the majority of parameters are well-defined with the exception of the eclipse phase transition rate (k), one of the half-saturation constants (K_E), and the CD8_M generation delay (τ_M).

the data, the model predicts that 17% of CD8_E transitioned to the memory class by 15 d pi. Additional insight into the regulation of the CD8$^+$ T cell response, results from the model fitting, and a comparison of the DD model and the CD8$^+$ T cell model are included in the Supporting Information.

Density-dependent infected cell clearance

To gain further insight into the nonlinear dynamics of CD8$^+$ T cell-mediated infected cell clearance, we plotted the clearance rate ($\delta_E(I_2, E) = \delta_E E/(K_{\delta_E} + I_2)$) as a function of infected cells (I_2) and CD8_E (E) (Figure 3). This confirmed that there is minimal contribution from CD8_E-mediated clearance to viral load kinetics or infected cell kinetics prior to 7 d pi (Figure 3A–C, markers a–b). At the initiation of the second decay phase (7 d pi), the clearance

rate is $\delta_E(I_2, E) = 3.5$/d (Figure 3A–B, marker c). As the infected cell density declines towards the half-saturation constant ($K_{\delta_E} = 4.3 \times 10^2$ cells), the clearance rate increases rapidly to a maximum of 4830/d (Figure 3A–C, markers d–g). The model predicts that there are 6×10^5 infected cells remaining at 7 d pi, which can be eliminated by $CD8_E$ in 6.7 h.

To explore how recovery time is altered by varying $CD8_E$ levels, we examined the resulting dynamics from increasing or decreasing the rate of $CD8_E$ expansion (η). When η was increased by 50%, the $CD8_E$ population increased by a substantial 670% (Figure S5). However, this was insufficient to significantly shorten the infection (8.4 d versus 7.8 d). The infection duration can be reduced if $CD8_E$ expansion began earlier (i.e., smaller τ_E; Figure S6). Although recovery is not significantly expedited by a larger $CD8_E$ population, the infection is dramatically prolonged if these cells are depleted (Figures 3D–E and S5). This *in silico* analysis revealed a bifurcation in recovery time, such that the infection is either resolved within ∼15 d pi or may last up to ∼45 d if $CD8_E$ are below a critical magnitude required to resolve the infection (Figure 3D–E). The critical number of total $CD8^+$ T cells needed for successful viral clearance was $\hat{E}_{\max}^{\text{crit}} = 7.4 \times 10^5$ CD8, which was 39.2% of the maximum number of $CD8^+$ T cells obtained from the best-fit solution (i.e., $\hat{E}_{\max} = 1.9 \times 10^6$ CD8). This corresponds to 17% of $CD8_E$ (i.e., $E_{\max}^{\text{crit}} = 2.3 \times 10^5$ $CD8_E$; Figure 3D–E). The model analysis indicated that decreasing the total number of $CD8^+$ T cells by as little as 0.1% from this critical level (i.e., 39.2% to 39.1%) lengthen the infection from 15 d pi to 25 d pi (Figure 3D).

Lung injury dynamics

To investigate the dynamics of infected cells, we quantified these cells and the progression and resolution of the lung injury using serial whole lung histomorphometry (Figure 4A). Antigen-positive areas of the lung ("active" lesions) were first detectable at 2 d pi (Figure 4A–B), which coincides with the peak in viral loads. The infected area continued to increase in a nonlinear manner until 6 d pi, whereas viral loads remained high until 7 d pi (Figure 1B). At this time, resolution of the infection began and the infected area declined at a rate of ∼28.7%/d between 6–7 d pi (Figure S7A). Few to no infected cells were present at 8 d pi (Figure 4A). Correspondingly, virus was undetectable in most animals by 8 d pi (Figure 1B). Because the percent active lesion is a reflection of the influenza-positive cells, we examined whether the $CD8^+$ T cell model accurately predicted these dynamics. In the model, the accumulated infection is defined by the cumulative area under the curve (CAUC) of the productively infected cells (I_2). Plotting the percent active lesion against the CAUC of I_2 shows that the model accurately

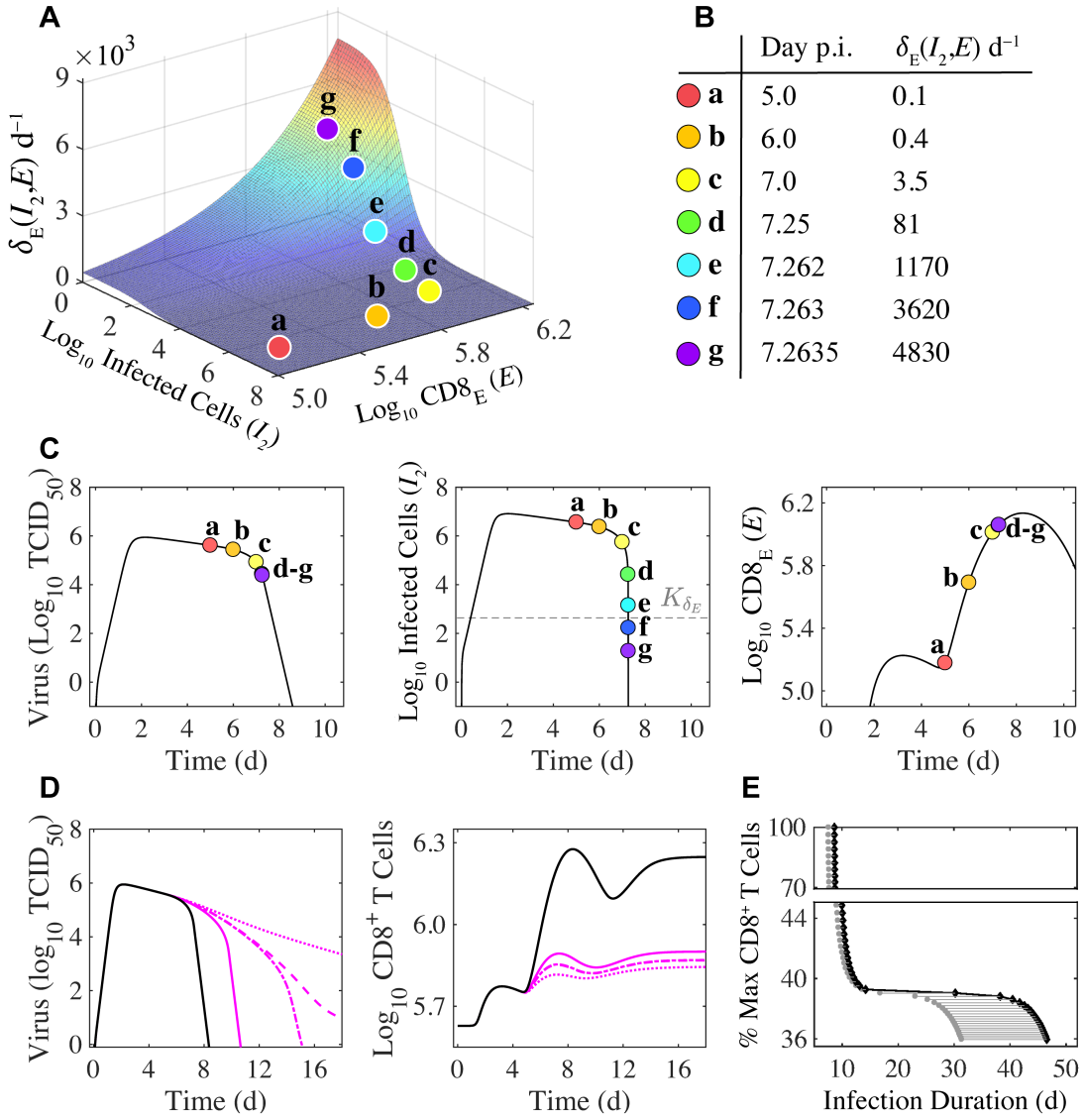

Figure 3. Density-dependent infected cell clearance by CD8$^+$ T cells and their impact on recovery time. (A) The rate of $CD8_E$-mediated infected cell clearance ($\delta_E(I_2, E) = \delta_E E/(K_{\delta_E} + I_2)$) plotted as a function of infected cells (I_2) and effector CD8$^+$ T cells (E; $CD8_E$). The colored markers (denoted a–g) indicate the infected cell clearance rate that corresponds to different time points during the infection for the best-fit solution. (B) Values of $\delta_E(I_2, E)$ for the indicated time points associated with the markers a–g. (C) Corresponding locations of the various $\delta_E(I_2, E)$ values (markers a–g) on the best-fit solution of the CD8$^+$ T cell model for virus (V), infected cells (I_2), and $CD8_E$ (E). (D) Solutions of the CD8$^+$ T cell model (Equations (1)–(6)) for virus (V) and total CD8$^+$ T cells ($\hat{E}$) using the best-fit parameters (black line) and when varying the $CD8_E$ expansion rate (η; magenta lines) to illustrate how different total CD8$^+$ T cell magnitudes alter infection duration. The magenta lines are solutions from when the percent $\hat{E}_{\max}$ relative to $\hat{E}_{\max}$ from the best-fit solution was 42% (solid line), 39.2% (dash-dotted line), 39.1% (dashed line), or 37% (dotted line). (E) The time at which infected cells reach the half-saturation constant ($I_2 = K_{\delta_E}$; gray circles) and the infection duration (time where $\log_{10} V = 0$; black diamonds) are shown for the various CD8$^+$ T cell magnitudes. The gray line between these points is the time required to eliminate K_{δ_E} infected cells and achieve complete resolution of the infection ($\log_{10} V = 0$).

reflects the cumulative infected cell dynamics and, thus, the infection progression within the lung (Figure 4B). Plotting the CAUC of I_2 for all parameter sets in the 95% CIs further illustrates the accuracy by showing that the heterogeneity in the histomorphometry data is captured (Figure 4B), which is larger than the heterogeneity in viral loads (Figure 1B).

Antigen-negative, previously-infected or damaged areas of the lung ("inactive" lesions) are evident beginning at 5 d pi (Figure 4A,C). This resolution of the infection continued from 5–8 d pi, causing a 14.6%/d increase in the area of inactive lesions (Figure S7B). Following this, healing of the injured lung is apparent as the inactive lesioned areas decline (-14.5%/d from 9–10 d pi; Figures 4C and S7B). These dynamics parallel the $CD8^+$ T cell dynamics (Figure 1B). Fitting a line to the $CD8^+$ T cell data from 5–8 d pi indicated that the influx rate is 4.7×10^5 cells/d (Figure S7C). Thus, the model estimates that every 100,000 $CD8^+$ T cells clear $\sim 3.1\%$ of the lung. During the $CD8^+$ T cell contraction phase (8–10 d pi; Figure 1B), a similar linear regression analysis suggested that these cells decline at a rate of $\sim 3.3 \times 10^5$ CD8/d (Figure S7C). Similar to the relation discussed above, the dynamics of the damaged areas of the lung corresponded precisely to the dynamics of the percent maximum $CD8_E$ (i.e., $E/E_{\max}$) in the model (Figure 4C). Further, adding the predicted dynamics for the active and inactive lesions agrees with the dynamics of the total percent lesion (Figure S8).

Weight loss predicts area of lung injured

To monitor disease progression, weight loss was measured daily throughout the course of infection (Figure 4D). During the first 5 d pi, animals gradually lost ~4% of their initial weight. This was followed by a sharper drop (8%) at 6 d pi. Animal weights increased slightly at 7 d pi (~6%) before reaching peak weight loss (10–14%) at 8 d pi. Following virus resolution, the animals' weights began to restore as the inactive lesions resolved (9–10 d pi; Figure 4D). We hypothesized that these weight loss dynamics may reflect the area of the lung impacted by the infection. Indeed, plotting weight loss together with the percent total (active and inactive) lesioned area of the lung revealed the similarity in their dynamics (Figure 4D-E). To further quantify their relationship, we plotted the percent weight loss against the percent total lesioned area and observed a nonlinear relation. Thus, we fit the saturating function $L = l_{\max} W^n/(W^n + K_w^n)$ to these data, where L is the percent total lesioned area, W is percent weight loss, $l_{\max}$ is the maximum rate of the interaction, K_w is the half-saturation constant, and n is the Hill coefficient. This function provided a close fit to the data ($R^2 = 0.9$; Figure 4E) with best-fit parameters $l_{\max}$=39.7% total lesioned area, K_w=2.6% weight loss, and $n = 5.2$.

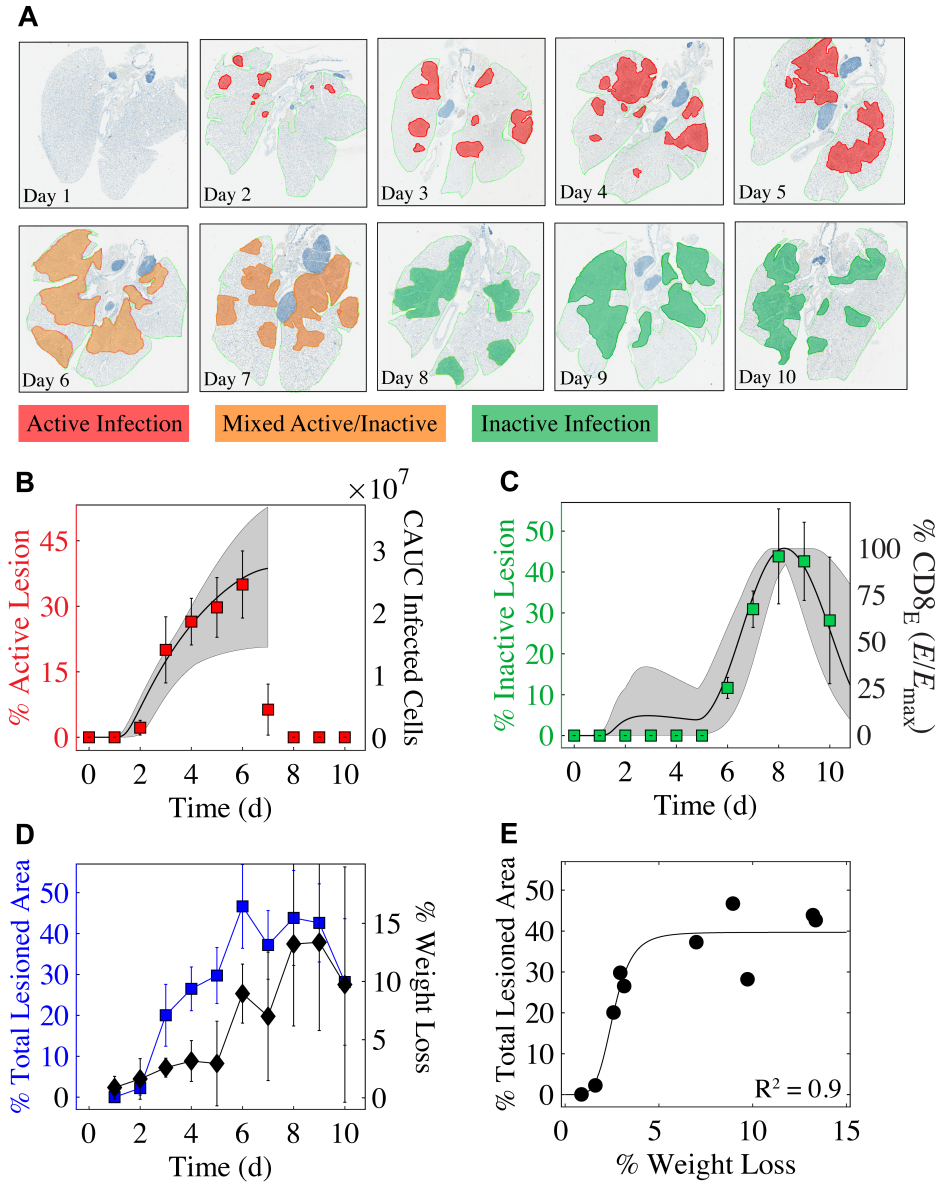

Figure 4. Histomorphometry of the IAV-infected lung and its relation to weight loss and model dynamics. (A) Whole lung sections with histomorphometry showing the areas of influenza NP-positive "active" lesions (red), "inactive" lesions with minimal antigen-positive debris (green), or mixed active and inactive regions (orange) throughout the infection. (B) Percent active lesion (red squares) plotted together with the cumulative area under the curve (CAUC) of the predicted infected cell dynamics (I_2) obtained from fitting the CD8$^+$ T cell model. The black line and gray shading are the curves generated using the best-fit parameters and the 95% CI parameters (Table 1), respectively. The line and shading stop where the CAUC of I_2 stops changing. (C) Percent inactive lesion (green squares) plotted together with the percent maximum $\mathrm{CD8_E}$ ($E/E_{\max}$) obtained from fitting the CD8$^+$ T cell model. (D) The combined percent active and inactive lesion (blue squares) plotted together with the percent weight loss (black diamonds) to illustrate their similar dynamics. (E) Fit of a saturating function ($L(W) = l_{\max} W^n/(K_w^n + W^n)$) to the mean percent total lesioned area (L) and mean weight loss (W) for all time points. The best-fit parameters were $l_{\max} = 39.7\%$ total lesioned area, $K_w = 2.6\%$ weight loss, and $n = 5.2$.

Discussion

Influenza A virus infections pose a significant threat to human health, and it is crucial to understand how the virus spreads within the respiratory tract, how specific immune responses contribute to infection control, and how these relate to disease progression. Although it has been difficult to directly relate these features, we circumvented the challenge by pairing comprehensive experimental data with robust mathematical models and analyses. Our iterative model-driven experiment approach [63,64] revealed important dynamic relations between virus, infected cells, CD8$^+$ T cells, lung damage, and weight loss (Figure 5). Identifying these nonlinear connections allows for more accurate interpretations of viral infection data and significant improvement in our ability to predict disease severity, the likelihood of complications, and therapeutic efficacy.

Our histomorphometric data provided the first quantification of the spread of influenza virus

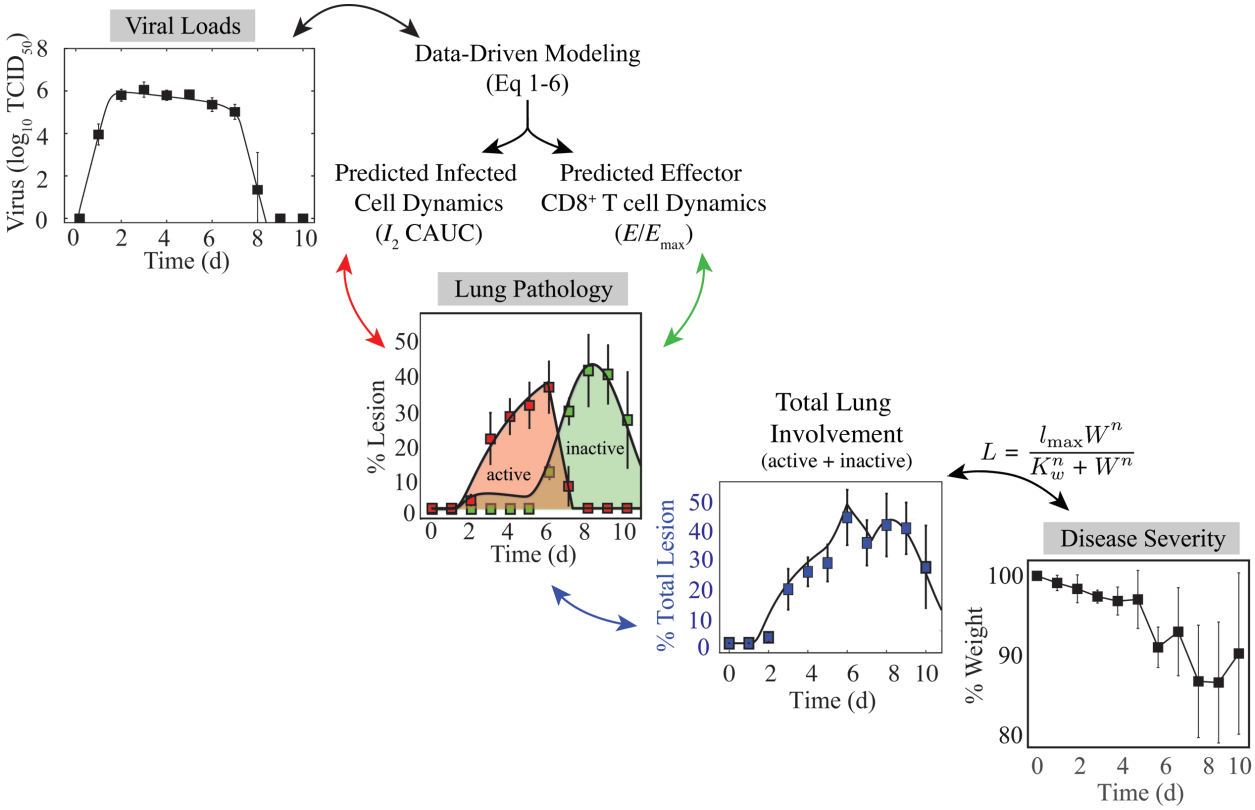

Figure 5. Connection between the kinetics of virus, infected cells, CD8$^+$ T cells, lung pathology, and disease severity. Viral loads and weight loss are the most easily measured data. Our analysis relates these through mathematical models. That is, given viral loads, the CD8$^+$ T cell model (Equations (1)–(6)) can be used to estimate the kinetics of infected cells and CD8$^+$ T cells. The cumulative area under the curve (CAUC) of the predicted infected cell dynamics (I_2) yields an estimate of the percent lung infected (active lesion) while the predicted relative CD8$_E$ dynamics (E/E_{max}) yields an estimate of the percent lung resolved (inactive lesion). The total amount of lung involved (% lung infected and % lung resolved) can then be used to estimate weight loss through the function $L(W)$. These connections can be reversed and weight loss used to predict viral load kinetics.

infection within the lung and the dynamics of lung injury. These data allowed us to validate our model's predicted infected cell dynamics and provide support that their density impacts the rate at which they are cleared by effector $CD8^+$ T cells ($CD8_E$) (Figure 4). Interestingly, $CD8^+$ T cell dynamics can be mostly replicated when assuming the density dependence lies within their expansion (Figure S1). Discriminating between these mechanisms is difficult *in vivo*, but the ability of the model in Equations (1)-(6) to capture the entire time course of $CD8_E$ dynamics is compelling. Regardless of the mechanism, we first detected this density-dependence in a model that excluded specific immune responses (i.e., Equations (S7)–(S10)) [15]. That model was a mathematically elegant way to capture the nonlinearity in the viral load decline, but it could not distinguish between different mechanisms of viral clearance. Here, we verified that the second viral clearance phase reflects $CD8^+$ T cell-mediated clearance, determined that their efficiency increases as more infected cells are removed, and identified the critical level needed for a timely recovery (Figure 3).

Several factors may contribute to the density-dependent change in the rate of $CD8_E$-mediated clearance. One possibility is that the slowed rate of clearance at high infected cell densities is due to a "handling time" effect, which represents the time required for an immune cell to remove an infected cell (e.g., as in [15, 27, 32, 65–68]). When $CD8_E$ interact with infected cells, a complex is formed for ∼20–40 min [35, 69–72]. Because $CD8_E$ could not interact with other infected cells during this time, the global rate of infected cell clearance would be lowest when infected cells outnumber $CD8_E$. In addition, contact by a single $CD8_E$ may be insufficient to remove an infected cell [31]. Infected cell clearance is more frequently observed after interactions with multiple $CD8_E$, with an average of 3.9 contact events either serially or simultaneously [31]. Thus, the high density of infected cells early in the infection reduces the probability that a single virus-infected cell would be targeted a sufficient number times to induce cell death. However, as $CD8_E$ accumulate and the density of infected cells decreases (Figure 3A), the probability of simultaneous interactions will increase. This should reduce the handling time required to remove of an infected cell and, thus, result in a higher efficiency. While this is a likely explanation, it is possible that spatial limitations also contribute, such that a high infected cell density may hinder $CD8^+$ T cells from reaching infected cells on the interior of the infected tissue. Crowding of immune cells at the periphery of infected lesions has been observed in other infections (e.g., in tuberculosis granulomas [73, 74]) and has been suggested in agent-based models of influenza virus infection [75].

The new knowledge about how the infection spreads throughout the lung also uncovered a

novel connection between the percent weight loss of an infected animal (i.e., disease severity) and the percent total area of the lung injured during the virus infection (Figure 4D–E). This discovery is significant because it suggests that disease severity is linked to the extent of lung injury, which we showed is directly connected to infected cell and $CD8_E$ kinetics (Figure 4B–C) and indirectly connected to viral load kinetics (Figure 5). Other studies utilizing histomorphometry data, although not quantitatively, corroborate the relationship between weight loss and lung involvement during IAV infection [12]. For example, animals treated with antivirals in various conditions (single or combination therapy and in immunocompetent or immunosuppressed hosts) demonstrated that, although viral loads are not always significantly reduced, the antiviral-induced reductions in weight loss corresponded to decreased infected areas of the lung [12, 45]. Examining the lung injury kinetics and its connection with weight loss in various infection settings (e.g., high versus low dose, different ages or sex, under therapy, other strains or viruses, etc.) and how innate responses contribute to the lung injury should improve our predictive capabilities. This may be particularly helpful in understanding the exacerbated morbidity and mortality in elderly individuals, where there is typically lower viral loads compared to adults coupled with increased weight loss, symptoms, and/or mortality within animal models [13, 14].

The nonlinear relations derived from the lung injury analysis (Figures 4–5) further provide a way to interpret and utilize weight loss data, which is the most readily available type of data and commonly used as a measure of disease severity in infection models. These results demonstrate significant potential for weight loss data to be used, analyzed, and interpreted within both modeling and experimental studies. In our data and others', there is a spike in weight loss, symptom score, and/or inflammation at ∼6 d pi [53, 57, 76, 77] (Figure 4D). Our data suggests that this may be due to $CD8_E$ infiltration and activity while the infection continues to spread. The subsequent increase in animal weights starting at 7 d pi is concurrent with the decline in infected lesions (Figure 4). Utilizing this observation and the function describing the correlation between the percent lung lesion and weight loss ($L(W)$; Figure 4E), the kinetics of the active and inactive lesioned areas can be directly estimated from weight loss data (Figure 5). Taking this one step further, the dynamics of the CAUC of the productively infected cells (I_2) and the relative $CD8_E$ can be obtained. Finally, the $CD8^+$ T cell model (Equations (1)–(6)) can be employed to estimate the viral load and $CD8^+$ T cell dynamics (Figure 5). These connections can be reversed to estimate disease severity (i.e., weight loss) from viral load data.

The model's 95% CI predictions of the lesioned area nicely captured the heterogeneity in the data (Figures 4 and S8), which is remarkable given the minimal variability in the virus and $CD8^+$

T cell data and model fit (Figure 1B). The differential heterogeneity suggests that small changes to viral loads can induce a significant changes in disease severity. Indeed, this has been observed when antivirals are administered [78–83] or when host responses are modified [84–86]. It may also indicate that viral loads are not a reliable measure of infection severity. This knowledge should also aid future studies seeking to estimate therapeutic efficacy or the effects of immune modulation. There was a slight over-estimation of the inactive lesion early in the infection (1–5 d pi, dark gray shading; Figure 4). This may suggest that the $CD8^+$ T cells present during this time do not have effector capabilities or are not virus-specific (Figure 4C). These cells could also be tissue resident T cells and/or T cells circulating in the blood.

Weight loss increases following infection resolution (8–9 d pi), which is likely attributed to $CD8^+$ T cell-mediated pathology (Figure 4C). This is supported by other studies that suggest a large number of $CD8^+$ T cells poses a risk of acute lung tissue injury [5–9]. According to our model predictions, excessive $CD8^+$ T cell numbers may augment disease progression yet do not improve recovery time (Figure S5). Instead, an earlier onset of $CD8_E$ proliferation (i.e., smaller τ_E) would be required to significantly shorten the infection (Figure S6). This aligns with evidence that hosts with adaptive immune responses primed by vaccine or prior infection recover more rapidly [87, 88]. While higher $CD8^+$ T cell numbers have little impact on viral kinetics, the model agrees with clinical and experimental studies from a wide range of host species that impaired $CD8^+$ T cell responses can prolong an IAV infection [17, 22, 26, 89–91]. That is, virus can persist for up to several weeks if $CD8^+$ T cell-mediated clearance is unsuccessful (Figure 3; [26,92,93]). The bifurcation in recovery time revealed by the model suggests that this may occur when the number of effector $CD8^+$ T cells are less than 2.3×10^5 $CD8_E$ (Figure 3D–E). This number is expected to vary depending on parameters like the rate of virus replication and the infected cell lifespan, which has been noted in another modeling study that detailed similar bifurcation behavior [94]. Although some previously published models also suggested delayed resolution with depleted $CD8^+$ T cell responses [17, 36, 37, 95], this bifurcation has not been observed and their estimated delays in recovery do not amount to the long-lasting infections in immunodeficient patients [26, 92, 93]. Further, although one model is able to match viral load kinetics in the absence of B cells or T cells [36], the result was contingent on the continuous abundance of susceptible cells that was caused by a reversion of an interferon-induced refractory state, which is not supported by experimental data [96]. Including innate responses or antibodies in our model may affect the parameter values, the predicted $CD8^+$ T cell threshold value, and/or the critical number of $CD8^+$ T cells required for recovery, but the close fit of the model and

estimation of the lung lesions suggests that the qualitative results would not change.

In addition to illuminating the connections between virus spread, virus clearance, the associated pathology, and the severity of disease, the histomorphometric data validated the model's infected cell dynamics (Figure 4B). The dynamics of susceptible and infected cells throughout the infection and the accuracy of the target cell limited approximation used within influenza viral kinetic models have been questioned for several years [64,97–102]. The ability of the model to accurately predict the histomorphometry data corroborates the use of this approximation, which assumes a limited number of available target cells and describes their decline by infection only. Although the slowing of virus spread is likely more dynamic and involves immune-mediated mechanisms, more complex dynamics are unnecessary to describe the data. Further, the model and data agree that there are few infected cells during the time when viral loads are growing most rapidly (0–2 d pi; Figures 1B and 4B). We previously used this information to derive approximations for the model and gain deeper insight into how each parameter influences the kinetics [103], which has helped numerous studies interpret their results [15, 17, 104, 105]. The data also supports the model's hypothesis that that there is minimal clearance of infected cells prior to $CD8_E$ infiltration (Figure 3A–B). The knowledge of the model's accuracy and of the spatial spread throughout the lung should aid investigation into the mechanisms that limit virus growth during the early stages of the infection.

Employing targeted model-driven experimental designs to examine and validate theoretical predictions like the ones presented here is pivotal to elucidating the mechanisms of infection spread and clearance [63, 64]. Examining other infections (e.g., coronaviruses) and modifications to the dynamics (e.g., high dose or antiviral therapy) will help refine the dynamical link between virus, host immune responses, and disease severity and identify its generalizability. Determining the factors that influence disease severity/weight loss is vital to understanding the disproportionate mortality in at-risk populations (e.g., elderly) and to improve therapeutic design. This is particularly important because current antivirals alleviate symptoms but do not effectively lower viral loads [78–83]. The predictive capabilities of validated models like the one here should prove useful in forecasting infection dynamics for a variety of scenarios. These tools and analyses provide a more meaningful interpretation of infection data, new ways to interpret weight loss data, and a deeper understanding of the progression and resolution of the disease, which will undoubtedly aid our ability to effectively combat influenza.

Methods and Materials

Ethics statement

All experimental procedures were performed under protocol O2A-020 approved by the Animal Care and Use Committee at St. Jude Children's Research Hospital under relevant institutional and American Veterinary Medical Association (AVMA) guidelines and were performed in a biosafety level 2 facility that is accredited by the American Association for Laboratory Animal Science (AALAS).

Mice

Adult (6 week old) female BALB/cJ mice were obtained from Jackson Laboratories (Bar Harbor, ME). Mice were housed in groups of 5 mice in high-temperature 31.2cm × 23.5cm × 15.2cm polycarbonate cages with isolator lids. Rooms used for housing mice were maintained on a 12:12-hour light:dark cycle at 22 ± 2°C with 50% humidity in the biosafety level 2 facility at St. Jude Children's Research Hospital (Memphis, TN). Prior to inclusion in the experiments, mice were allowed at least 7 d to acclimate to the animal facility such that they were 7 weeks old at the time of infection. Laboratory Autoclavable Rodent Diet (PMI Nutrition International, St. Louis, MO) and autoclaved water were available ad libitum. All experiments were performed under an approved protocol and in accordance with the guidelines set forth by the Animal Care and Use Committee at St. Jude Children's Research Hospital.

Infectious agents

All experiments were done using the mouse adapted influenza A/Puerto Rico/8/34 (H1N1) (PR8).

Infection experiments

The viral infectious dose ($TCID_{50}$) was determined by interpolation using the method of Reed and Muench [106] using serial dilutions of virus on Madin-Darby canine kidney (MDCK) cells (obtained from Dr. Jonathan McCullers). Mice were intranasally inoculated with 75 $TCID_{50}$ PR8 diluted in 100µl of sterile PBS. Mice were weighed at the onset of infection and each subsequent day to monitor illness and mortality. Mice were euthanized if they became moribund or lost 30% of their starting body weight. For viral load and $CD8^+$ T cell quantification, experiments were repeated three times to ensure reproducibility and two complete experiments

(10 animals per time point) were used for these studies. Histomorphometry was performed on five animals per time point.

Lung harvesting for viral and cellular dynamics

Mice were euthanized by CO_2 asphyxiation. Lungs were aseptically harvested, washed three times in PBS, and placed in 500µl sterile PBS. Whole lungs were digested with collagenase (1mg/ml, Sigma C0130), and physically homogenized by syringe plunger against a 40µm cell strainer. Cell suspensions were centrifuged at 4°C, 500xg for 7 min. The supernatants were used to determine the viral titers ($TCID_{50}$) by serial dilutions on MDCK monolayers. Following red blood cell lysis, cells were washed in MACS buffer (PBS, 0.1M EDTA, 0.01M HEPES, 5mM EDTA and 5% heat-inactivated FBS). Cells were then counted with trypan blue exclusion using a Cell Countess System (Invitrogen, Grand Island, NY) and prepared for flow cytometric analysis as indicated below.

Lung titers

For each animal, viral titers were obtained using serial dilutions on MDCK monolayers and normalized to the total volume of lung homogenate supernatant. The resulting viral loads are shown in Figure 1B and were previously published and utilized for calibration of the density-dependent model (Equations (S7)–(S10) (Supplementary Information)) [15].

Flow cytometric analysis

Flow cytometry (LSRII Fortessa; Becton Dickinson, San Jose, CA) was performed on the cell pellets after incubation with 200µl of a 1:2 dilution of Fc block (human-γ globulin) on ice for 30 min, followed by surface marker staining with anti-mouse antibodies: CD11c (eFluor450, eBioscience), CD11b (Alexa700, BD Biosciences), Ly6G (PerCp-Cy5.5, Biolegend), Ly6C (APC, eBioscience), F4/80 (PE, eBioscience), CD3e (PE-Cy7, BD Biosciences or BV785, Biolegend), CD4 (PE-Cy5, BD Biosciences), CD8α (BV605, BD Biosciences), DX5 (APC-Cy7, Biolegend or APC-e780, Affymetrix, Inc) and MHC-II (FITC, eBioscience). The data were analyzed using FlowJo 10.4.2 (Tree Star, Ashland, OR) where viable cells were gated from a forward scatter/side scatter plot and singlet inclusion. Following neutrophil ($Ly6G^{hi}$) and subsequent macrophage ($CD11c^{hi}F4/80^{hi}$) exclusion, $CD8^+$ T cells were gated as $CD3e^+CD8\alpha^+CD4^-DX5^-$. The absolute numbers of $CD8^+$ T cells was calculated based on viable events analyzed by flow cytometry as related to the total number of viable cells per sample. We chose to use the kinetics of the total

number of CD8$^+$ T cells rather than virus-specific CD8$^+$ T cells because virus-specific subsets often have varying dynamics (e.g., as in [13]) and would complicate the model and potentially skew the results. The gating strategy is shown in Figure S9.

Lung histomorphometry and immunohistochemistry

The lungs from IAV infected mice were fixed via intratracheal infusion and then immersion in 10% buffered formalin solution. Tissues were paraffin embedded, sectioned, and stained for influenza virus using a primary goat polyclonal antibody (US Biological, Swampscott, MA) against influenza A, USSR (H1N1) at 1:1000 and a secondary biotinylated donkey anti-goat antibody (sc-2042; Santa Cruz Biotechnology, Santa Cruz, CA) at 1:200 on tissue sections subjected to antigen retrieval for 30 minutes at 98°C. The extent of virus spread was quantified by capturing digital images of whole-lung sections stained for viral antigen using an Aperio ScanScope XT Slide Scanner (Aperio Technologies, Vista, CA) then manually outlining defined fields. Alveolar areas containing virus antigen-positive pneumocytes were highlighted in red (defined as "active" infection), whereas lesioned areas containing minimal or no virus antigen-positive debris were highlighted in green (defined as "inactive" infection). Lesions containing a mix of virus antigen-positive and antigen-negative pneumocytes were highlighted in orange (defined as "mixed" infection). The percentage of each defined lung field was calculated using the Aperio ImageScope software. Representative images and quantitative analyses of viral spread and lung pathology during IAV infection are shown in Figure 4A–C.

CD8$^+$ T cell model

To examine the contribution of CD8$^+$ T cells to the biphasic viral load decay, we expanded the density-dependent (DD) model (Equations (S7)–(S10) (Supplementary Information)) to include two mechanisms of infected cell clearance (non-specific clearance (δ) and CD8$^+$ T cell-mediated clearance ($\delta_E(I_2, E)$)) and two CD8$^+$ T cell populations: effector (E, denoted $\mathrm{CD8_E}$) and memory (E_M, denoted $\mathrm{CD8_M}$) CD8$^+$ T cells. The model is given by Equations (1)–(6).

$$\frac{dT}{dt} = -\beta TV \tag{1}$$

$$\frac{dI_1}{dt} = \beta TV - kI_1 \tag{2}$$

$$\frac{dI_2}{dt} = kI_1 - \delta I_2 - \delta_E(I_2, E)I_2 \tag{3}$$

$$\frac{dV}{dt} = pI_2 - cV \tag{4}$$

$$\frac{dE}{dt} = \xi(E)I_2 + \eta E I_2(t - \tau_E) - d_E E \tag{5}$$

$$\frac{dE_M}{dt} = \zeta E(t - \tau_M) \tag{6}$$

In this model, target cells become infected with virus at rate βV per day. Once infected, cells enter an eclipse phase (I_1) before transitioning at rate k per day to a productively-infected state (I_2). These infected cells produce virus at rate p $mathrmTCID_{50}$ per infected cell per day, and virus is cleared at rate c per day. Virus-producing infected cells (I_2) are cleared by non-specific mechanisms (e.g., apoptosis and/or innate immune responses) at a constant rate δ per day. Innate immune responses were excluded from the model because the viral load data is linear during the time where they act (2–7 d pi) and, thus, additional equations cannot improve the fit. Productively infected cells are cleared by $CD8_E$ at rate $\delta_E(I_2, E) = \delta_E E/(K_{\delta_E} + I_2)$ per day, where the rate of infected cell clearance is δ_E/K_{δ_E} per $CD8_E$ per day and K_{δ_E} is the half-saturation constant. The $CD8_E$-mediated clearance rate ($\delta_E(I_2, E)$) is dependent on the density of infected cells and is similar to the infected cell clearance term in the DD model (see Equation (S9)) [15]. Similar density-dependent forms have also been used in models that describe the $CD8^+$ T cell response to other virus infections [32,34,65]. Models that exclude this density-dependence were examined, but these models resulted in a poor fit to the data. This is due in part to the infiltration of $CD8^+$ T cells from 3–5 d pi (Figure 1). We did examine a model that excluded these dynamics and included $CD8^+$ T cell expansion as a density-dependent function (e.g., $\eta E I_2(t - \tau_E)/(K_I + I_2)$) while keeping a linear rate of CD8-mediated infected cell clearance ($\delta_E E I_2$) (Equations (S1)–(S6); Figure S1). This model was adapted from other published models [60,61,107] and can produce similar dynamics from 6-10 d pi, but there is less experimental support for this model.

The model assumes that $CD8_E$ infiltrate the lung proportional to infected cells at rate $\xi(E) = \xi/(K_E + E)$ $CD8_E$ per cell per day, which is down-regulated by the $CD8_E$ already present in the lung. The associated half-saturation constant is K_E. Similar terms for $CD8_E$ regulation have been used in modeling HIV infections [34, 108] and in models that examined $CD8^+$ T cell proliferation mechanisms [109]. In our model, $CD8_E$ expansion occurs at rate η per infected cell per day with time delay τ_E. This term accounts for local $CD8_E$ proliferation in the lung [110,111] and migration of $CD8_E$ from secondary lymphoid organs [20,112–114]. The delay may signify the time it takes $CD8_E$ to become activated by antigen presenting cells, differentiate, proliferate, and/or migrate to the infection site. The lung $CD8_E$ population declines due to cell

death and/or emigration at rate d_E per day. These cells transition to $CD8_M$ (E_M) at rate ζ $CD8_M$ per $CD8_E$ per day after τ_M days. The model schematic and fit to the viral load and $CD8^+$ T cell data are in Figure 1.

Parameter estimation

Given a parameter set θ, the cost $C(\theta)$ was minimized across parameter ranges using an Adaptive Simulated Annealing (ASA) global optimization algorithm [15] to compare experimental and predicted values of $\log_{10}$ $TCID_{50}$/lung virus (V) and of $\log_{10}$ total $CD8^+$ T cells/lung ($\hat{E} = E + E_M + \hat{E}_0$, where $\hat{E}_0$ is the initial number of $CD8^+$ T cells at 0 d pi). The cost function is defined by

$$C(\theta) = \sum_{i,j}(V(\theta,t_i) - v_{i,j})^2 + s_E \left[\sum_{i,j}(\hat{E}(\theta,t_i) - e_{i,j})^2 + \sum_i \sqrt{\gamma_i}\left(\frac{\hat{E}(\theta,t_{i+1}) - \hat{E}(\theta,t_{i-1})}{t_{i+1} - t_{i-1}} - \frac{1}{\gamma_i}\sum_j \frac{e_{i+1,j} - e_{i-1,j}}{t_{i+1} - t_{i-1}}\right)^2\right],$$

where $(t_i, v_{i,j})$ is the viral load data, $(t_i, e_{i,j})$ is the $CD8^+$ T cell data, and $V(\theta,t_i)$ and $\hat{E}(\theta,t_i)$ are the corresponding model predictions. Here, $s_E = (v_{\max} - v_{\min})/(e_{\max} - e_{\min})$ is a scaling factor, and $\gamma_i = J_{i+1}J_{i-1}$ where J_i is the number of observations at time t_i. Errors of the $\log_{10}$ data were assumed to be normally distributed. To explore and visualize the regions of parameters consistent with the model, we fit Equations (1)–(6) to 2000 bootstrap replicates of the data. If the fit was within $\chi^2 = 0.05$ of the best-fit and the CD8 derivative was not a statistical outlier as determined by the function *isoutlier*, then the bootstrap was considered successful [15, 104, 115]. For each best-fit estimate, we provide 95% confidence intervals (CI) obtained from the bootstrap replicates (Table 1). All calculations were performed in Python using the *simanneal* package [116] followed by a L-BFGS-B [117,118] deterministic minimization through SciPy's *minimize* function. SciPy integrate.ode using *lsoda* and PyDDE [119] were used as the ODE and DDE solvers.

Estimated parameters included the rates of virus infection (β), virus production (p), virus clearance (c), eclipse phase transition (k), non-specific infected cell clearance (δ), $CD8_E$-mediated infected cell clearance (δ_E), half-saturation constants (K_{δ_E} and K_E), $CD8_E$ infiltration (ξ), $CD8_E$ expansion (η), delay in $CD8_E$ expansion (τ_E), $CD8_E$ clearance (d_E), $CD8_M$ generation (ζ), delay in $CD8_M$ generation (τ_M), and the baseline number of $CD8^+$ T cells ($\hat{E}_0$).

Bounds were placed on the parameters to constrain them to physically realistic values. Because biological estimates are not available for all parameters, ranges were set reasonably large based on preliminary results and previous estimates [15]. The rate of infection (β) was allowed to vary between $10^{-6} - 10^{-1}$ TCID_{50}^{-1} d^{-1}, and the rate of virus production (p) between $10^{-1} - 10^{3}$ TCID_{50} cell^{-1} d^{-1}. Bounds for the virus clearance rate (c) were 1 d^{-1} ($t_{1/2} = 16.7$ h) and 10^{3} d^{-1} ($t_{1/2} = 1$ min). To insure biological feasibility, the lower and upper bounds for the eclipse phase transition rate (k) were $4 - 6$ d^{-1} as done previously [15].

The rate of non-specific infected cell clearance (δ) was given limits of $0.05 - 1$ d^{-1}. The CD8_{E}-mediated infected cell clearance rate (δ_E) varied between $0.01 - 2$ cells $\text{CD8}_{\text{E}}^{-1}$ d^{-1}, and the associated half-saturation constant (K_{δ_E}) was bounded between $10^2 - 10^6$ cells. The upper bound of δ_E was chosen to maintain the convergence of δ to nonzero values. Bounds for the rate of CD8_{E} infiltration (ξ) were $10^2 - 10^6$ CD8_{E}^2 cell^{-1} d^{-1}, and bounds for the half-saturation constant (K_E) were $10^3 - 10^6$ CD8_{E}. The CD8_{E} expansion rate (η) varied between $10^{-8} - 10^{-6}$ cell^{-1} d^{-1}, and the delay in CD8_{E} expansion (τ_E) between 2–6 d. The rate of CD8_{E} clearance (d_E) had limits of $0.05 - 2$ d^{-1}. The rate of CD8_{M} generation (ζ) varied between $0.01 - 1$ CD8_{M} $\text{CD8}_{\text{E}}^{-1}$ d^{-1}, and the delay in CD8_{M} generation (τ_M) varied between 3–4 d. Larger bounds were examined for this parameter, however, the parameter is non-identifiable and a small range was required for convergence. Bounds for the baseline number of CD8^+ T cells ($\hat{E}_0$) were set to the upper and lower values of the data at 0 d pi ($3.0 \times 10^5 - 5.3 \times 10^5$ CD8).

The initial number of target cells ($T(0)$) was set to 10^7 cells [15,104,115]. The initial number of infected cells $I_1(0)$ was set to 75 cells to reflect an initial dose of 75 TCID_{50} [15]. We previously found that estimating $I_1(0)$, fixing $V(0) = 75$ TCID_{50}, or estimating $V(0)$ did not improve the fit and could not be statistically justified [15]. The initial number of productively infected cells ($I_2(0)$), the initial free virus ($V(0)$), and the initial number of CD8_{E} ($E(0)$) and CD8_{M} ($E_M(0)$) were set to 0.

Linear regression

The function *polyfit* in MATLAB was used to perform linear regression on the percent active lesioned area, the percent inactive lesioned area, and the CD8^+ T cells during the expansion phase (5–8 d pi) and the contraction phase (9–10 d pi). Linear fits are shown in Figure S7.

Area under the curve

The function *cumtrapz* in MATLAB was used to estimate the cumulative area under the curve (CAUC) of the infected cells (I_2) for the best-fit model solution.

Acknowledgments

This work was supported by NIH grant AI100946, AI125324, and AI139088 and ALSAC. We thank Alan Perelson for his helpful comments, and Robert Michael for technical assistance.

References

1. Thompson WW, Shay DK, Weintraub E, Brammer L, Bridges CB, Cox NJ, et al. Influenza-associated hospitalizations in the United States. JAMA-J Am Med Assoc. 2004;292(11):1333–1340.

2. Simonsen L, Fukuda K, Schonberger LB, Cox NJ. The impact of influenza epidemics on hospitalizations. J Infect Dis. 2000;181(3):831–837.

3. Taubenberger JK, Morens DM. The pathology of influenza virus infections. Annu Rev Path Mech Dis. 2008;3:499–522.

4. Medina RA, García-Sastre A. Influenza A viruses: New research developments. Nat Rev Microbiol. 2011;9(8):590–603.

5. Duan S, Thomas PG. Balancing immune protection and immune pathology by $CD8^+$ T-cell responses to influenza infection. Front Immunol. 2016;7:25.

6. Moskophidis D, Kioussis D. Contribution of virus-specific $CD8^+$ cytotoxic T cells to virus clearance or pathologic manifestations of influenza virus infection in a T cell receptor transgenic mouse model. J Exp Med. 1998;188(2):223–232.

7. Mauad T, Hajjar LA, Callegari GD, da Silva LF, Schout D, Galas FR, et al. Lung pathology in fatal novel human influenza A (H1N1) infection. Am J Respir Crit Care Med. 2010;181(1):72–79.

8. Rygiel TP, Rijkers ES, de Ruiter T, Stolte EH, van der Valk M, Rimmelzwaan GF, et al. Lack of CD200 enhances pathological T cell responses during influenza infection. J Immunol. 2009; p. jimmunol–0900252.

9. La Gruta NL, Kedzierska K, Stambas J, Doherty PC. A question of self-preservation: Immunopathology in influenza virus infection. Immunol Cell Biol. 2007;85(2):85–92.

10. Boon AC, Finkelstein D, Zheng M, Liao G, Allard J, Klumpp K, et al. H5N1 influenza virus pathogenesis in genetically diverse mice is mediated at the level of viral load. MBio. 2011;2(5):e00171–11.

11. Granados A, Peci A, McGeer A, Gubbay J. Influenza and rhinovirus viral load and disease severity in upper respiratory tract infections. J Clin Virol. 2017;86:14–19.

12. Marathe BM, Wong SS, Vogel P, Garcia-Alcalde F, Webster RG, Webby RJ, et al. Combinations of oseltamivir and T-705 extend the treatment window for highly pathogenic influenza A (H5N1) virus infection in mice. Sci Rep. 2016;6:26742.

13. Toapanta FR, Ross TM. Impaired immune responses in the lungs of aged mice following influenza infection. Respir Res. 2009;10(1):112.

14. Smith CA, Kulkarni U, Chen J, Goldstein DR. Influenza virus inoculum volume is critical to elucidate age-dependent mortality in mice. Aging Cell. 2019; p. e12893.

15. Smith AP, Moquin DJ, Bernhaurova V, Smith AM. Influenza virus infection model with density dependence supports biphasic viral decay. Front Microbiol. 2018;9:1554. doi:10.3389/fmicb.2018.01554.

16. Baccam P, Beauchemin C, Macken CA, Hayden FG, Perelson AS. Kinetics of influenza A virus infection in humans. J Virol. 2006;80(15):7590–7599.

17. Miao H, Hollenbaugh JA, Zand MS, Holden-Wiltse J, Mosmann TR, Perelson AS, et al. Quantifying the early immune response and adaptive immune response kinetics in mice infected with influenza A virus. J Virol. 2010;84(13):6687–6698.

18. Carrat F, Vergu E, Ferguson NM, Lemaitre M, Cauchemez S, Leach S, et al. Time lines of infection and disease in human influenza: A review of volunteer challenge studies. Am J Epidemiol. 2008;167(7):775–785.

19. Srivastava B, Błażejewska P, Heßmann M, Bruder D, Geffers R, Mauel S, et al. Host genetic background strongly influences the response to influenza a virus infections. PLoS One. 2009;4(3):e4857.

20. Zhang N, Bevan MJ. $CD8^+$ T cells: Foot soldiers of the immune system. Immunity. 2011;35(2):161–168.

21. Chen X, Liu S, Goraya MU, Maarouf M, Huang S, Chen JL. Host immune response to influenza A virus infection. Front Immunol. 2018;9:320.

22. McMichael A, Gotch F, Noble G, Beare P. Cytotoxic T-cell immunity to influenza. N Engl J Med. 1983;309(1):13–17.

23. La Gruta NL, Turner SJ. T cell mediated immunity to influenza: mechanisms of viral control. Trends Immunol. 2014;35(8):396–402.

24. Kreijtz J, Fouchier R, Rimmelzwaan G. Immune responses to influenza virus infection. Virus Res. 2011;162(1-2):19–30.

25. Fang M, Sigal LJ. Antibodies and $CD8^+$ T cells are complementary and essential for natural resistance to a highly lethal cytopathic virus. J Immunol. 2005;175(10):6829–6836.

26. Wang Z, Wan Y, Qiu C, Quinones-Parra S, Zhu Z, Loh L, et al. Recovery from severe H7N9 disease is associated with diverse response mechanisms dominated by $CD8^+$ T cells. Nat Commun. 2015;6:6833.

27. Graw F, Regoes RR. Investigating CTL mediated killing with a 3D cellular automaton. PLoS Comput Biol. 2009;5(8):e1000466.

28. Wiedemann A, Depoil D, Faroudi M, Valitutti S. Cytotoxic T lymphocytes kill multiple targets simultaneously via spatiotemporal uncoupling of lytic and stimulatory synapses. P Natl Acad Sci. 2006;103(29):10985–10990.

29. Merrill SJ. Foundations of the use of an enzyme-kinetic analogy in cell-mediated cytotoxicity. Math Biosci. 1982;62(2):219–235.

30. Caramalho Í, Faroudi M, Padovan E, Müller S, Valitutti S. Visualizing CTL/melanoma cell interactions: Multiple hits must be delivered for tumour cell annihilation. J Cell Mol Med. 2009;13(9b):3834–3846.

31. Halle S, Keyser KA, Stahl FR, Busche A, Marquardt A, Zheng X, et al. In vivo killing capacity of cytotoxic T cells is limited and involves dynamic interactions and T cell cooperativity. Immunity. 2016;44(2):233–245.

32. Gadhamsetty S, Marée AF, Beltman JB, de Boer RJ. A general functional response of cytotoxic T lymphocyte-mediated killing of target cells. Biophys J. 2014;106(8):1780–1791.

33. Ganusov VV, Barber DL, De Boer RJ. Killing of targets by $CD8^+$ T cells in the mouse spleen follows the law of mass action. PLoS One. 2011;6(1):e15959.

34. De Boer RJ, Perelson AS. Target cell limited and immune control models of HIV infection: A comparison. J Theor Biol. 1998;190(3):201–214.

35. Perelson A, Bell G. Delivery of lethal hits by cytotoxic T lymphocytes in multicellular conjugates occurs sequentially but at random times. J Immunol. 1982;129(6):2796–2801.

36. Cao P, Wang Z, Yan AWC, McVernon J, Xu J, Heffernan JM, et al. On the role of $CD8^+$ T cells in determining recovery time from influenza virus infection. Front Immunol. 2016;7.

37. Lee HY, Topham DJ, Park SY, Hollenbaugh J, Treanor J, Mosmann TR, et al. Simulation and prediction of the adaptive immune response to influenza A virus infection. J Virol. 2009;83(14):7151–7165.

38. Price I, Mochan-Keef ED, Swigon D, Ermentrout GB, Lukens S, Toapanta FR, et al. The inflammatory response to influenza A virus (H1N1): An experimental and mathematical study. J Theor Biol. 2015;374:83–93.

39. Bautista E, Chotpitayasunondh T, Gao Z, Harper S, Shaw M, Uyeki T, et al. Clinical aspects of pandemic 2009 influenza A (H1N1) virus infection. New Engl J Med. 2010;362(18):1708–1719.

40. van de Sandt CE, Bárcena M, Koster AJ, Kasper J, Kirkpatrick CJ, Scott DP, et al. Human $CD8^+$ T Cells damage noninfected epithelial cells during influenza virus infection in vitro. Am J Respir Cell Mol Biol. 2017;57(5):536–546.

41. Manicassamy B, Manicassamy S, Belicha-Villanueva A, Pisanelli G, Pulendran B, García-Sastre A. Analysis of in vivo dynamics of influenza virus infection in mice using a GFP reporter virus. P Natl Acad Sci. 2010;107(25):11531–11536.

42. Tran V, Moser LA, Poole DS, Mehle A. Highly sensitive real-time in vivo imaging of an influenza reporter virus reveals dynamics of replication and spread. J Virol. 2013; p. JVI–02381.

43. Karlsson EA, Meliopoulos VA, Savage C, Livingston B, Mehle A, Schultz-Cherry S. Visualizing real-time influenza virus infection, transmission and protection in ferrets. Nat Commun. 2015;6:6378.

44. Luker KE, Luker GD. Bioluminescence imaging of reporter mice for studies of infection and inflammation. Antivir Res. 2010;86(1):93–100.

45. Marathe BM, Mostafa HH, Vogel P, Pascua PNQ, Jones JC, Russell CJ, et al. A pharmacologically immunosuppressed mouse model for assessing influenza B virus pathogenicity and oseltamivir treatment. Antivir Res. 2017;148:20–31.

46. Sartorius A, Lu Q, Vieira S, Tonnellier M, Lenaour G, Goldstein I, et al. Mechanical ventilation and lung infection in the genesis of air-space enlargement. Crit Care. 2007;11(1):R14.

47. Zachariadis O, Cassidy J, Brady J, Mahon BP. $\gamma\delta$ T cells regulate the early inflammatory response to Bordetella pertussis infection in the murine respiratory tract. Infect Immunity. 2006;74(3):1837–1845.

48. Lee CS, Lee JH. Dynamics of clinical symptoms in patients with pandemic influenza A (H1N1). Clin Microbiol Infect. 2010;16(4):389–390.

49. Han A, Poon JL, Powers JH, Leidy NK, Yu R, Memoli MJ. Using the influenza patient-reported outcome (FLU-PRO) diary to evaluate symptoms of influenza viral infection in a healthy human challenge model. BMC Infect Dis. 2018;18(1):353.

50. Trammell RA, Toth LA. Markers for predicting death as an outcome for mice used in infectious disease research. Comparative Med. 2011;61(6):492–498.

51. Bouvier NM, Lowen AC. Animal models for influenza virus pathogenesis and transmission. Viruses. 2010;2(8):1530–1563.

52. Parzych EM, DiMenna LJ, Latimer BP, Small JC, Kannan S, Manson B, et al. Influenza virus specific $CD8^+$ T cells exacerbate infection following high dose influenza challenge of aged mice. Biomed Res Int. 2013; p. 876314.

53. Huang CT, Hung CY, Chen TC, Lin CY, Lin YC, Chang CS, et al. Rapamycin adjuvant and exacerbation of severe influenza in an experimental mouse model. Sci Rep. 2017;7(1):4136.

54. Lauder SN, Taylor PR, Clark SR, Evans RL, Hindley JP, Smart K, et al. Paracetamol reduces influenza-induced immunopathology in a mouse model of infection without compromising virus clearance or the generation of protective immunity. Thorax. 2011; p. thx–2010.

55. Xu L, Yoon H, Zhao MQ, Liu J, Ramana CV, Enelow RI. Cutting edge: Pulmonary immunopathology mediated by antigen-specific expression of TNF-α by antiviral $CD8^+$ T cells. J Immunol. 2004;173(2):721–725.

56. Ostler T, Davidson W, Ehl S. Virus clearance and immunopathology by $CD8^+$ T cells during infection with respiratory syncytial virus are mediated by IFN-γ. Eur J Immunol. 2002;32(8):2117–2123.

57. Lu J, Duan X, Zhao W, Wang J, Wang H, Zhou K, et al. Aged mice are more resistant to influenza virus infection due to reduced inflammation and lung pathology. Aging Dis. 2018;9(3):358.

58. McAuley JL, Hornung F, Boyd KL, Smith AM, McKeon R, Bennink J, et al. Expression of the 1918 influenza A virus PB1-F2 enhances the pathogenesis of viral and secondary bacterial pneumonia. Cell Host & Microbe. 2007;2(4):240–249.

59. Baral S, Antia R, Dixit NM. A dynamical motif comprising the interactions between antigens and CD8 T cells may underlie the outcomes of viral infections. Proceedings of the National Academy of Sciences. 2019;116(35):17393–17398. doi:10.1073/pnas.1902178116.

60. Bonhoeffer S, Rembiszewski M, Ortiz GM, Nixon DF. Risks and benefits of structured antiretroviral drug therapy interruptions in HIV-1 infection. Aids. 2000;14(15):2313–2322.

61. Conway JM, Perelson AS. Post-treatment control of HIV infection. P Natl Acad Sci. 2015;112(17):5467–5472.

62. Kaech SM, Hemby S, Kersh E, Ahmed R. Molecular and functional profiling of memory CD8 T cell differentiation. Cell. 2002;111(6):837–851.

63. Smith AM. Validated models of immune response to virus infection. Curr Opin Sys Biol. 2018;12:46–52.

64. Smith AM. Host-pathogen kinetics during influenza infection and coinfection: Insights from predictive modeling. Immuno Rev. 2018;285(1):97–112.

65. Li Y, Handel A. Modeling inoculum dose dependent patterns of acute virus infections. J Theor Biol. 2014;347:63–73.

66. Le D, Miller JD, Ganusov VV. Mathematical modeling provides kinetic details of the human immune response to vaccination. Front Cell Infect Microbiol. 2015;4:177.

67. Pilyugin SS, Antia R. Modeling immune responses with handling time. B Math Biol. 2000;62(5):869–890.

68. Smith AM, McCullers JA, Adler FR. Mathematical model of a three-stage innate immune response to a pneumococcal lung infection. J Theor Biol. 2011;276(1):106 – 116. doi:10.1016/j.jtbi.2011.01.052.

69. Mempel TR, Pittet MJ, Khazaie K, Weninger W, Weissleder R, von Boehmer H, et al. Regulatory T cells reversibly suppress cytotoxic T cell function independent of effector differentiation. Immunity. 2006;25(1):129–141.

70. Deguine J, Breart B, Lemaître F, Di Santo JP, Bousso P. Intravital imaging reveals distinct dynamics for natural killer and $CD8^+$ T cells during tumor regression. Immunity. 2010;33(4):632–644.

71. Zagury D, Bernard J, Thierness N, Feldman M, Berke G. Isolation and characterization of individual functionally reactive cytotoxic T lymphocytes: Conjugation, killing and recycling at the single cell level. Eur J Immunol. 1975;5(12):818–822.

72. Yannelli J, Sullivan J, Mandell G, Engelhard V. Reorientation and fusion of cytotoxic T lymphocyte granules after interaction with target cells as determined by high resolution cinemicrography. J Immunol. 1986;136(2):377–382.

73. Ulrichs T, Kosmiadi GA, Trusov V, Jörg S, Pradl L, Titukhina M, et al. Human tuberculous granulomas induce peripheral lymphoid follicle-like structures to orchestrate local host defence in the lung. J Pathol. 2004;204(2):217–228.

74. Russell DG, Cardona PJ, Kim MJ, Allain S, Altare F. Foamy macrophages and the progression of the human tuberculosis granuloma. Nat Immunol. 2009;10(9):943.

75. Levin D, Forrest S, Banerjee S, Clay C, Cannon J, Moses M, et al. A spatial model of the efficiency of T cell search in the influenza-infected lung. J Theor Biol. 2016;398:52–63.

76. Music N, Reber AJ, Lipatov AS, Kamal RP, Blanchfield K, Wilson JR, et al. Influenza vaccination accelerates recovery of ferrets from lymphopenia. PLoS One. 2014;9(6):e100926.

77. Kugel D, Kochs G, Obojes K, Roth J, Kobinger GP, Kobasa D, et al. Intranasal administration of alpha interferon reduces seasonal influenza A virus morbidity in ferrets. J Virol. 2009;83(8):3843–3851.

78. Jefferson T, Jones MA, Doshi P, Del Mar CB, Hama R, Thompson M, et al. Neuraminidase inhibitors for preventing and treating influenza in healthy adults and children. Sao Paulo Med J. 2014;132(4):256–257.

79. Hayden FG, Sugaya N, Hirotsu N, Lee N, de Jong MD, Hurt AC, et al. Baloxavir marboxil for uncomplicated influenza in adults and adolescents. New England Journal of Medicine. 2018;379(10):913–923.

80. Treanor JJ, Hayden FG, Vrooman PS, Barbarash R, Bettis R, Riff D, et al. Efficacy and safety of the oral neuraminidase inhibitor oseltamivir in treating acute influenza: A randomized controlled trial. JAMA-J Am Med Assoc. 2000;283(8):1016–1024.

81. Moscona A. Neuraminidase inhibitors for influenza. New Engl J Med. 2005;353(13):1363–1373.

82. Gubareva LV, Kaiser L, Hayden F. Influenza virus neuraminidase inhibitors. Lancet. 2000;355(9206):827–835.

83. Koshimichi H, Ishibashi T, Kawaguchi N, Sato C, Kawasaki A, Wajima T. Safety, tolerability, and pharmacokinetics of the novel anti-influenza agent baloxavir marboxil in healthy adults: phase I study findings. Clin Drug Investig. 2018;38(12):1189–1196.

84. Channappanavar R, Fehr AR, Vijay R, Mack M, Zhao J, Meyerholz DK, et al. Dysregulated type I interferon and inflammatory monocyte-macrophage responses cause lethal pneumonia in SARS-CoV-infected mice. Cell Host Microbe. 2016;19(2):181–193.

85. Szretter KJ, Gangappa S, Belser JA, Zeng H, Chen H, Matsuoka Y, et al. Early control of H5N1 influenza virus replication by the type I interferon response in mice. J Virol. 2009;83(11):5825–5834.

86. Iwasaki T, Nozima T. Defense mechanisms against primary influenza virus infection in mice: I. The roles of interferon and neutralizing antibodies and thymus dependence of interferon and antibody production. J Immunol. 1977;118(1):256–263.

87. Duan S, Meliopoulos VA, McClaren JL, Guo XZJ, Sanders CJ, Smallwood HS, et al. Diverse heterologous primary infections radically alter immunodominance hierarchies and clinical outcomes following H7N9 influenza challenge in mice. PLoS Pathog. 2015;11(2):e1004642.

88. Weinfurter JT, Brunner K, Capuano III SV, Li C, Broman KW, Kawaoka Y, et al. Cross-reactive T cells are involved in rapid clearance of 2009 pandemic H1N1 influenza virus in nonhuman primates. PLoS Pathog. 2011;7(11):e1002381.

89. Yap K, Ada G. Cytotoxic T cells in the lungs of mice infected with an influenza A virus. Scand J Immunol. 1978;7(1):73–80.

90. Wells M, Albrecht P, Ennis F. Recovery from a viral respiratory infection. I. Influenza pneumonia in normal and T-deficient mice. J Immunol. 1981;126(3):1036–1041.

91. Bender BS, Croghan T, Zhang L, Small P. Transgenic mice lacking class I major histocompatibility complex-restricted T cells have delayed viral clearance and increased mortality after influenza virus challenge. J Exp Med. 1992;175(4):1143–1145.

92. Eichelberger M, Allan W, Zijlstra M, Jaenisch R, Doherty P. Clearance of influenza virus respiratory infection in mice lacking class I major histocompatibility complex-restricted $CD8^+$ T cells. J Exp Med. 1991;174(4):875–880.

93. Hou S, Doherty P, Zijlstra M, Jaenisch R, Katz J. Delayed clearance of Sendai virus in mice lacking class I MHC-restricted $CD8^+$ T cells. J Immunol. 1992;149(4):1319–1325.

94. Yates AJ, Van Baalen M, Antia R. Virus replication strategies and the critical CTL numbers required for the control of infection. PLoS Comput Biol. 2011;7(11):e1002274.

95. Dobrovolny HM, Reddy MB, Kamal MA, Rayner CR, Beauchemin CA. Assessing mathematical models of influenza infections using features of the immune response. PLoS One. 2013;8(2):e57088.

96. Borden EC, Murphy FA. The interferon refractory state: in vivo and in vitro studies of its mechanism. J Immunol. 1971;106(1):134–142.

97. Smith AM, Perelson AS. Influenza A virus infection kinetics: Quantitative data and models. WIREs Sys Biol Med. 2011;3(4):429–445. doi:10.1002/wsbm.129.

98. Beauchemin C, Handel A. A review of mathematical models of influenza A infections within a host or cell culture: Lessons learned and challenges ahead. BMC Public Health. 2011;11(Suppl 1):S7.

99. Ahmed H, Moore J, Manicassamy B, Garcia-Sastre A, Handel A, Antia R. Mathematical analysis of a mouse experiment suggests little role for resource depletion in controlling influenza infection within host. arXiv:170502565 [q-bio]. 2017;.

100. Gallagher M, Brooke C, Ke R, Koelle K. Causes and Consequences of Spatial Within-Host Viral Spread. Viruses. 2018;10(11):627.

101. Boianelli A, Nguyen V, Ebensen T, Schulze K, Wilk E, Sharma N, et al. Modeling influenza virus infection: a roadmap for influenza research. Viruses. 2015;7(10):5274–5304.

102. Handel A, Liao L, Beauchemin C. Progress and trends in mathematical modelling of influenza A virus infections. Curr Opin Sys Biol. 2018;12:30–36.

103. Smith AM, Adler FR, Perelson AS. An accurate two-phase approximate solution to an acute viral infection model. J Math Biol. 2010;60(5):711–726.

104. Smith AM, Adler FR, McAuley JL, Gutenkunst RN, Ribeiro RM, McCullers JA, et al. Effect of 1918 PB1-F2 expression on influenza A virus infection kinetics. PLoS Comput Biol. 2011;7(2):e1001081.

105. Holder BP, Beauchemin CA. Exploring the effect of biological delays in kinetic models of influenza within a host or cell culture. BMC Public Health. 2011;11(1):S10.

106. Reed LJ, Muench H. A simple method of estimating fifty percent endpoints. Am J Epidemiol. 1938;27(3):493–497.

107. Baral S, Antia R, Dixit NM. A dynamical motif comprising the interactions between antigens and CD8 T cells may underlie the outcomes of viral infections. bioRxiv. 2019; p. 540054.

108. Müller V, Marée AF, De Boer RJ. Small variations in multiple parameters account for wide variations in HIV–1 set–points: A novel modelling approach. Proc R Soc Lond B Biol Sci. 2001;268(1464):235–242.

109. De Boer RJ, Perelson AS. Towards a general function describing T cell proliferation. J Theor Biol. 1995;175(4):567–576.

110. McGill J, Legge KL. Cutting edge: Contribution of lung-resident T cell proliferation to the overall magnitude of the antigen-specific CD8 T cell response in the lungs following murine influenza virus infection. J Immunol. 2009;183(7):4177–4181.

111. Lawrence CW, Ream RM, Braciale TJ. Frequency, specificity, and sites of expansion of $CD8^+$ T cells during primary pulmonary influenza virus infection. J Immunol. 2005;174(9):5332–5340.

112. Bedoui S, Gebhardt T. Interaction between dendritic cells and T cells during peripheral virus infections: a role for antigen presentation beyond lymphoid organs? Curr Opin Immunol. 2011;23(1):124–130.

113. Wu H, Kumar A, Miao H, Holden-Wiltse J, Mosmann TR, Livingstone AM, et al. Modeling of influenza-specific $CD8^+$ T cells during the primary response indicates that the spleen is a major source of effectors. J Immunol. 2011;187(9):4474–4482.

114. Kang SS, Herz J, Kim JV, Nayak D, Stewart-Hutchinson P, Dustin ML, et al. Migration of cytotoxic lymphocytes in cell cycle permits local MHC I–dependent control of division at sites of viral infection. J Exp Med. 2011;208(4):747–759.

115. Smith AM, Adler FR, Ribeiro RM, Gutenkunst RN, McAuley JL, McCullers JA, et al. Kinetics of coinfection with influenza A virus and *Streptococcus pneumoniae*. PLoS Pathog. 2013;9(3):e1003238–e1003238.

116. Perry M. simanneal 0.4.1; 2018. Available from: `https://pypi.python.org/pypi/simanneal`.

117. Byrd RH, Lu P, Nocedal J, Zhu C. A limited memory algorithm for bound constrained optimization. SIAM J Sci Comput. 1995;16(5):1190–1208.

118. Zhu C, Byrd RH, Lu P, Nocedal J. Algorithm 778: L-BFGS-B: Fortran subroutines for large-scale bound-constrained optimization. ACM T Math Software. 1997;23(4):550–560.

119. Cairns BJ. PyDDE 0.2.2; 2008. Available from: `https://pypi.python.org/pypi/PyDDE`.